

# Hybrid perovskite films approaching the radiative limit with over 90% photoluminescence quantum efficiency

Ian L. Braly<sup>1,4</sup>, Dane W. deQuilettes<sup>2,4</sup>, Luis M. Pazos-Outón<sup>3</sup>, Sven Burke<sup>2</sup>, Mark E. Ziffer<sup>2</sup>, David S. Ginger<sup>2\*</sup> and Hugh W. Hillhouse<sup>1\*</sup>

**Reducing non-radiative recombination in semiconducting materials is a prerequisite for achieving the highest performance in light-emitting and photovoltaic applications. Here, we characterize both external and internal photoluminescence quantum efficiency and quasi-Fermi-level splitting of surface-treated hybrid perovskite (CH<sub>3</sub>NH<sub>3</sub>PbI<sub>3</sub>) thin films. With respect to the material bandgap, these passivated films exhibit the highest quasi-Fermi-level splitting measured to date, reaching  $97.1 \pm 0.7\%$  of the radiative limit, approaching that of the highest performing GaAs solar cells. We confirm these values with independent measurements of internal photoluminescence quantum efficiency of  $91.9 \pm 2.7\%$  under 1 Sun illumination intensity, setting a new benchmark for these materials. These results suggest hybrid perovskite solar cells are inherently capable of further increases in power conversion efficiency if surface passivation can be combined with optimized charge carrier selective interfaces.**

Organic–inorganic lead halide perovskites are promising semiconducting materials for a range of optoelectronic and electronic applications<sup>1,2</sup>. Their excellent performance in photovoltaic devices is often attributed to their high absorption coefficients<sup>3</sup>, long charge carrier diffusion lengths and lifetimes<sup>4,5</sup>, band-like charge carrier transport<sup>6</sup>, and high fractions of radiative recombination<sup>7–9</sup>. The latter is particularly important for light-emitting applications as well as photovoltaics, where ideal devices operate in the radiative limit<sup>10</sup>. As this limit is approached, all avoidable charge carrier recombination pathways are eliminated, and only radiative recombination remains<sup>11</sup>. As such, any non-radiative recombination reduces the steady-state, non-equilibrium carrier concentrations in the conduction and valence bands, and thus reduces the difference between the quasi-Fermi levels of these two bands ( $\Delta\mu = E_F^{\text{CB}} - E_F^{\text{VB}}$ ) and the resulting maximum achievable open-circuit voltage ( $V_{\text{OC}}$ )<sup>12,13</sup>. Therefore, when assessing the fundamental limitations of a new material, one of the most important considerations is determining whether the material can demonstrate a high fraction of radiative recombination relative to other recombination pathways<sup>14</sup>. For example, although Si has been deployed as a successful commercial technology and has recently achieved a record power conversion efficiency of 90% of its limiting efficiency<sup>15,16</sup>, it has demonstrated internal photoluminescence quantum efficiencies (PLQEs) ( $\eta_{\text{int}}$ ) just exceeding 20% (ref. 17), which at present limits its open-circuit voltage to 88% of its radiative limit open-circuit voltage<sup>18,19</sup>. On the other hand, GaAs, which holds the record power conversion efficiency for a single-junction solar cell at 28.8%, has demonstrated  $\eta_{\text{int}}$  as high as 99.7%<sup>20</sup>.

Although perovskites have shown rapid improvements in device performance over the last seven years, the pace appears to be slowing in single-junction cells<sup>8</sup>, as often happens as technologies mature and approach fundamental limits. A pivotal question now

lies in determining the guiding principles to fabricate more efficient devices to approach the theoretical efficiency limit. A similar situation occurred for GaAs, where device efficiencies were static for twenty years and the efficiency jumped by ~2.4% (percentage points) in a very short amount of time. Those improvements have been attributed primarily to improvements in  $V_{\text{OC}}$ , due to an increased understanding of the importance of luminescence extraction<sup>19</sup>. One might conclude that similar light-extraction improvements should be sought in perovskites, as reported short-circuit current densities have been reported to reach 92% of their theoretical maxima in state-of-the-art devices<sup>8</sup>, while  $V_{\text{OC}}$  and fill factors are more typically only ~87% or less of expected limits<sup>8,21</sup>.

The task of achieving high PLQEs has been challenging for solution-processed semiconductors due to the formation of both bulk and surface defects, which serve as non-radiative recombination centres. For thin-film perovskite layers, external PLQEs ( $\eta_{\text{ext}}$ ) at 1 Sun equivalent photon flux are typically <15% (refs 7,22), which can be increased by changing the outcoupling efficiency<sup>7</sup>. Although outcoupling is one promising avenue, there is an increasing amount of evidence suggesting that defects at surfaces and surface recombination velocities must be reduced to achieve the highest  $\eta_{\text{ext}}$  and therefore allow devices to operate at efficiencies close to the radiative limit<sup>23–25</sup>. While surface passivation strategies were essential in the development of leading semiconductor technologies such as Si and GaAs<sup>26,27</sup>, perovskite surface chemistry remains relatively unexplored by comparison and is expected to be an important consideration in achieving optimized devices<sup>28</sup>.

Lewis bases have been shown to passivate the surfaces of CH<sub>3</sub>NH<sub>3</sub>PbI<sub>3</sub> (ref. 24). Furthermore, we have recently shown that electron-donating molecules such as *n*-triethylphosphine oxide (TOPO) bind to the surface of CH<sub>3</sub>NH<sub>3</sub>PbI<sub>3</sub> perovskite and reduce non-radiative recombination<sup>5</sup>. These films demonstrated  $\eta_{\text{ext}}$

<sup>1</sup>Department of Chemical Engineering, Clean Energy Institute, and Molecular Engineering & Sciences Institute, University of Washington, Seattle, WA, USA. <sup>2</sup>Department of Chemistry, University of Washington, Seattle, WA, USA. <sup>3</sup>Electrical Engineering and Computer Sciences Department, University of California, Berkeley, CA, USA. <sup>4</sup>These authors contributed equally: Ian L. Braly, Dane W. deQuilettes. \*e-mail: [ginger@chem.washington.edu](mailto:ginger@chem.washington.edu); [h2@uw.edu](mailto:h2@uw.edu)

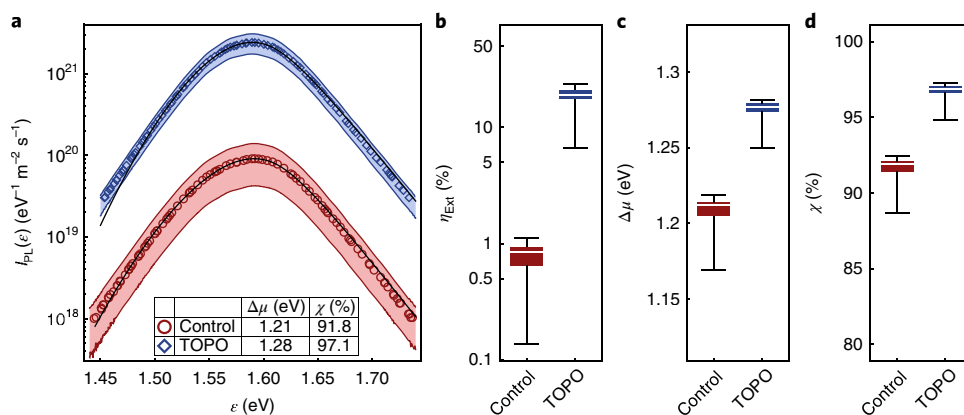


**Fig. 1 | Absolute intensity photoluminescence spectra of control and TOPO-treated  $\text{CH}_3\text{NH}_3\text{PbI}_3$  films deposited on an Au back-reflector substrate measured in air.** **a**, Log-scale photoluminescence spectra with fits to the data (black lines) using the generalized Planck model. Shaded regions: 95% confidence intervals for the spatial variation within the sample ( $N=121$ ). Quasi-Fermi-level splitting ( $\Delta\mu$ ) and per cent of radiative limit quasi-Fermi-level splitting ( $\chi$ ) are shown in the inset table. **b–d**, Parameter spatial statistics (min, first quartile, median, third quartile, and max;  $N=121$ ) of the control film and the TOPO-treated film obtained from fits of the spectra in **a**, showing  $\eta_{\text{ext}}$ ,  $\Delta\mu$  and  $\chi$ , respectively. Other fit parameters are reported in the Supplementary Information and Supplementary Fig. 1.

values as high as 35% at 1 Sun equivalent photon flux. This result is extremely encouraging considering the low escape probabilities (in the range of ~5.5–12.5%, as predicted by several groups), implying that  $\eta_{\text{int}}$  is probably much higher<sup>7,29,30</sup>.

We independently measured the quasi-Fermi-level splitting ( $\Delta\mu$ ),  $\eta_{\text{ext}}$  and  $\eta_{\text{int}}$  for solution-processed  $\text{CH}_3\text{NH}_3\text{PbI}_3$  perovskite thin films both before and after chemical surface passivation. We used a photoluminescence spectrometer (calibrated to measure absolute intensity and minimize spectral aberration) to measure  $\Delta\mu = 1.28 \pm 0.01$  eV after surface passivation, which is  $97.1 \pm 0.7\%$  of the radiative limit  $\Delta\mu$ , and is the highest value reported for a perovskite so far. We also used an integrating sphere to measure  $\eta_{\text{ext}} = 37.0 \pm 1.4\%$ , and calculated  $\eta_{\text{int}}$  by fitting experimental data with a detailed ray optics model that predicts the external PLQE as a function of parasitic loss<sup>20</sup>, and obtained a value of  $\eta_{\text{int}} = 91.9 \pm 2.7\%$ . Finally, we calculated the non-radiative and radiative rate coefficients of the untreated and TOPO-treated film to predict a power conversion efficiency improvement from 24.3 to 27.9%, which can be explained primarily by increases in  $V_{\text{OC}}$  and the fill factor.

These improvements relative to the control films are of comparable magnitude to those leading to the record GaAs solar cells<sup>31</sup>. This ultrahigh  $\Delta\mu$  suggests that surface passivation implemented with ideal contacts will be useful in overcoming Si efficiency records and in approaching efficiencies only achieved by GaAs.

### Determination of quasi-Fermi-level splitting

We used confocal photoluminescence spectroscopy to study  $\text{CH}_3\text{NH}_3\text{PbI}_3$  films before and after surface passivation. We prepared the perovskite precursor solution by mixing lead acetate and methylammonium iodide in dimethylformamide, then spin-coated this solution on a gold back-reflector substrate with a  $\text{SiO}_x$  insulating layer<sup>32</sup>. We note that this type of geometry closely resembles a typical structure for a perovskite-based photovoltaic device with Au serving as a back contact<sup>33</sup>. Sister samples were subsequently surface-treated with a dilute (0.025 M) solution of TOPO in chlorobenzene. We have previously shown that TOPO treatment reduces non-radiative recombination and is primarily confined to the surface, does not lead to any quantifiable changes in the film structure, and probably forms a new bond upon interaction with the perovskite surface<sup>5</sup>.

To determine the maximum achievable open-circuit voltage ( $V_{\text{OC}} = \Delta\mu/q$ ), we extracted  $\Delta\mu$  by performing a fit of the absolute

intensity photoluminescence spectrum to an expression based on the generalized Planck radiation law, as described in our previous work<sup>13</sup>. The equation relates the external spectral flux of radiative emission to the conduction-band and valence-band quasi-Fermi levels,  $E_{\text{F}}^{\text{CB}}$  and  $E_{\text{F}}^{\text{VB}}$ , and the spectral absorptivity,  $a$ :

$$I_{\text{PL}}(\epsilon) = \left\{ \frac{2\pi\epsilon^2}{h^3c^2} \right\} \times \left\{ \frac{1}{\exp\left(\frac{\epsilon - (E_{\text{F}}^{\text{CB}} - E_{\text{F}}^{\text{VB}})}{kT}\right) - 1} \right\} \times \{a(\epsilon, E_{\text{F}}^{\text{CB}}, E_{\text{F}}^{\text{VB}}, T)\} \quad (1)$$

where  $\epsilon$  is the photon energy in eV, and  $I_{\text{PL}}$  is the spectral photoluminescence emission flux in units of photons/( $\text{m}^2\text{s eV}$ ). Importantly, equation (1) is compatible with absorption coefficient models that include sub-gap states (see Supplementary Section 1 for additional details and assumptions). Although this is essential for describing the band-band emission peak shape for semiconductors that exhibit potential fluctuations (such as  $\text{Cu}(\text{In,Ga})\text{Se}_2$  and  $\text{Cu}_2\text{ZnSnSe}_4$ ), it is also required for fitting the photoluminescence peak shape from near-perfect semiconductors such as GaAs that also exhibit Urbach tails<sup>13</sup>. The method above, which fits the entire photoluminescence emission spectrum, avoids pitfalls associated with other techniques for extracting  $E_{\text{F}}^{\text{CB}} - E_{\text{F}}^{\text{VB}} = \Delta\mu$  from photoluminescence such as the high-energy tail fitting procedure<sup>34</sup>, as well as the common approach derived by Ross based on  $\eta_{\text{ext}}$  (ref. 35; see Supplementary Section 1 for details about each  $\Delta\mu$  determination method). A distinct advantage of the method detailed here is that it can be used to reveal the functional form of sub-gap tail states (see Supplementary Sections 2 and 3 for details of the absorption coefficient model, fitting procedure; Supplementary Figs. 1–3).

We measured the external PLQE of a representative control sample and TOPO-treated film at 1 Sun equivalent illumination intensity (continuous-wave,  $60 \text{ mW cm}^{-2}$  at 532 nm, see Supplementary Section 4 for details). Figure 1a shows the control (red) and treated (blue) photoluminescence spectra on an absolute scale (calibrated to a black-body source; for details see Supplementary Section 5 and Supplementary Figs. 5–7) with best fits to the data (black lines) obtained using equation (1). The untreated film exhibited an

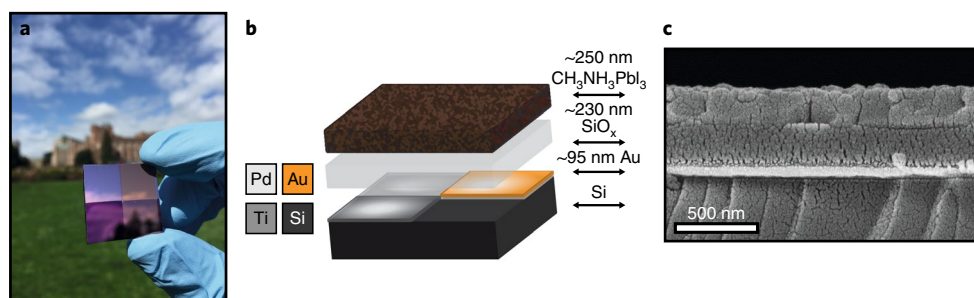


**Fig. 2 | Image and schematic diagram of multi-metal back-reflector substrates for determining the internal PLQE.** **a**, Photograph of the multi-metal back-reflector substrate before perovskite deposition. **b**, Schematic showing a multi-metal back-reflector substrate configuration; ~95 nm of Au, Pd and Ti were evaporated in separate quadrants on a Si wafer, a 230 nm insulating SiO<sub>x</sub> layer was evaporated on top of the metals, then a 250 nm layer of perovskite was spin-coated to complete the sample. **c**, Cross-sectional scanning electron microscopy (SEM) image of the Si/Au/SiO<sub>x</sub>/perovskite back-reflector sample.

average  $\eta_{\text{ext}}$  of  $0.92 \pm 0.50\%$  (Fig. 1b) and spatially averaged  $\Delta\mu$  of  $1.21 \pm 0.02$  eV ( $N=121$ , 95% confidence) (Fig. 1c), which is typical for films prepared by the lead acetate route and comparable to values reported for the highest performing devices<sup>8</sup>. Next, we fitted the photoluminescence spectrum of a TOPO surface-passivated film, demonstrating an average  $\eta_{\text{ext}}$  of  $20.3 \pm 5.6\%$ , and extracted  $\Delta\mu = 1.28 \pm 0.01$  eV ( $N=121$ , 95% confidence). Because the photoluminescence of polycrystalline perovskite thin films is known to be spatially heterogeneous<sup>36</sup>, we report spatial averages, with the error intervals primarily reflecting the spatial heterogeneity in the film. These fitted  $\Delta\mu$  data are consistent with the values determined using the relationship derived by Ross based on  $\eta_{\text{ext}}$  and the radiative limit  $\Delta\mu$  (ref. <sup>35</sup>), and similar to the method detailed by Bauer<sup>34</sup>, where only the high-energy tail of the photoluminescence is fitted (Supplementary Table 1).

The magnitude of this improvement in  $\Delta\mu$  after TOPO treatment is impressive considering the logarithmic dependence of  $V_{\text{OC}}$  on  $\eta_{\text{ext}}$  (Supplementary equation (6)), where enhancements on a similar scale led to record efficiencies for GaAs<sup>31</sup>. Because the  $V_{\text{OC}}$  deficit for a given material depends on its bandgap, we used the modelled bandgap energy to calculate the radiative limit  $\Delta\mu$  and compare to the observed values of  $\Delta\mu$ . The radiative limit is defined as the detailed balance limit for a material accounting for its real absorptivity spectrum. We note that this limit is dependent on several factors including film thickness and total sub-gap absorptivity (Supplementary Fig. 4). Using the extracted bandgap of 1.60 eV, Fig. 1d shows that the control film achieved  $91.7 \pm 1.3\%$  of the radiative limit  $\Delta\mu$ , again consistent with high-quality, untreated films that have been implemented in state-of-the-art devices<sup>8</sup>. The  $\Delta\mu$  is enhanced to  $97.1 \pm 0.7\%$  (Fig. 1d) of the radiative limit  $\Delta\mu$  after TOPO surface passivation, which is higher than any device reported so far (Supplementary Section 6 and Supplementary Fig. 8). We calculate this value to be only 40 meV less than the radiative limit  $\Delta\mu$  (Supplementary Figs. 2 and 3 and Discussion). To put this in context, if a passivated hybrid perovskite film such as the one studied here can be successfully implemented in a device with appropriate selective contacts, then the resulting device ( $V_{\text{OC}} = 1.28$  V) would be comparable to the 1.122 V achieved by the world record GaAs<sup>16,37</sup>, which is 96.2% of the Shockley–Queisser limit  $V_{\text{OC}}$  for GaAs<sup>11</sup>.

### Determination of internal PLQE

The high optoelectronic quality of the TOPO-treated CH<sub>3</sub>NH<sub>3</sub>PbI<sub>3</sub> measured in this work could only be obtained from samples with very high  $\eta_{\text{int}}$ . For example, the  $\eta_{\text{ext}}$  of planar perovskite films can be significantly lower than the  $\eta_{\text{int}}$  as a result of the low outcoupling efficiencies ( $\sim 10\%$ )<sup>7,22</sup>, which result from the narrow escape cone due to the perovskite refractive index ( $n \sim 2.6$ ). Additionally, determining the ratio between radiative and non-radiative recombination can

be obscured by reabsorption of emitted photons. For these reasons, and to better gauge the quality of the films prepared in this work, we determine  $\eta_{\text{int}}$  by adapting a method previously applied to high-quality GaAs by measuring  $\eta_{\text{ext}}$  of the perovskite film with varying back-surface parasitic absorption<sup>20</sup>.

In this model,  $\eta_{\text{ext}}$  can be related to  $\eta_{\text{int}}$  and parasitic losses from non-ideal back-surface reflectivity with equation (2) (after ref. <sup>20</sup>; see Supplementary Section 7 and Supplementary Figs. 9–15 for assumptions):

$$\eta_{\text{ext}} = \frac{\eta_{\text{int}}/2n^2}{\eta_{\text{int}}/2n^2 + (1 - \eta_{\text{int}}) + L/4\alpha_0 d_0} \quad (2)$$

In equation (2),  $n$  is the average refractive index (Supplementary Section 2.6 and Supplementary Fig. 13) over the perovskite emission band,  $\alpha_0$  is the average band-edge absorption coefficient ( $1.20 \times 10^4$  cm<sup>-1</sup>) over the perovskite emission band,  $d_0$  is the measured absorber thickness (250 nm), and  $L$  is the loss factor, defined as  $L = 1 - \text{Reflectivity}$ . Using these definitions, we calculate  $\alpha_0 d_0$  to be 0.3 and hold this value constant for fitting. Briefly, equation (2) describes the fraction of external radiative recombination over the total recombination. The factors that reduce the photon flux from the front surface include non-radiative recombination within the active layer of the film as well as parasitic absorption outside the active layer. Assuming that waveguiding modes are not present in the back-reflector stack (Supplementary Fig. 11), photon recycling and total internal reflections at steady state just represent re-emission into the pool of trapped luminescent photons and contribute no net gain or loss and are therefore included by default in equation (2)<sup>20</sup>.

Figure 2 shows the samples used for measuring  $\eta_{\text{int}}$ , which comprise a thin ~250 nm perovskite active layer spin-coated on top of a four-quadrant metal mirror with four different metal samples (Fig. 2a). The procedure involved measuring  $\eta_{\text{ext}}$  for a number of samples with well-characterized quantities of parasitic absorption outside the active layer<sup>20</sup>, and in our case the varying reflectivity of the back mirrors, Pd, Au, Ti and Si, played the role of varying the parasitic loss term. A SiO<sub>x</sub> layer between the mirrors and the perovskite layer prevented electronic interaction and near-field quenching with the metals.

To determine the optical losses suffered by the perovskite photoluminescence (780 nm centre, 44 nm full-width at half-maximum, FWHM) within the stack, we characterized the total optical loss within these substrates before perovskite deposition by measuring the angle-averaged reflectivity across the objective excitation/collection cone using a 790 nm light-emitting diode (LED; 23 nm FWHM) and a calibrated wide-field microscope

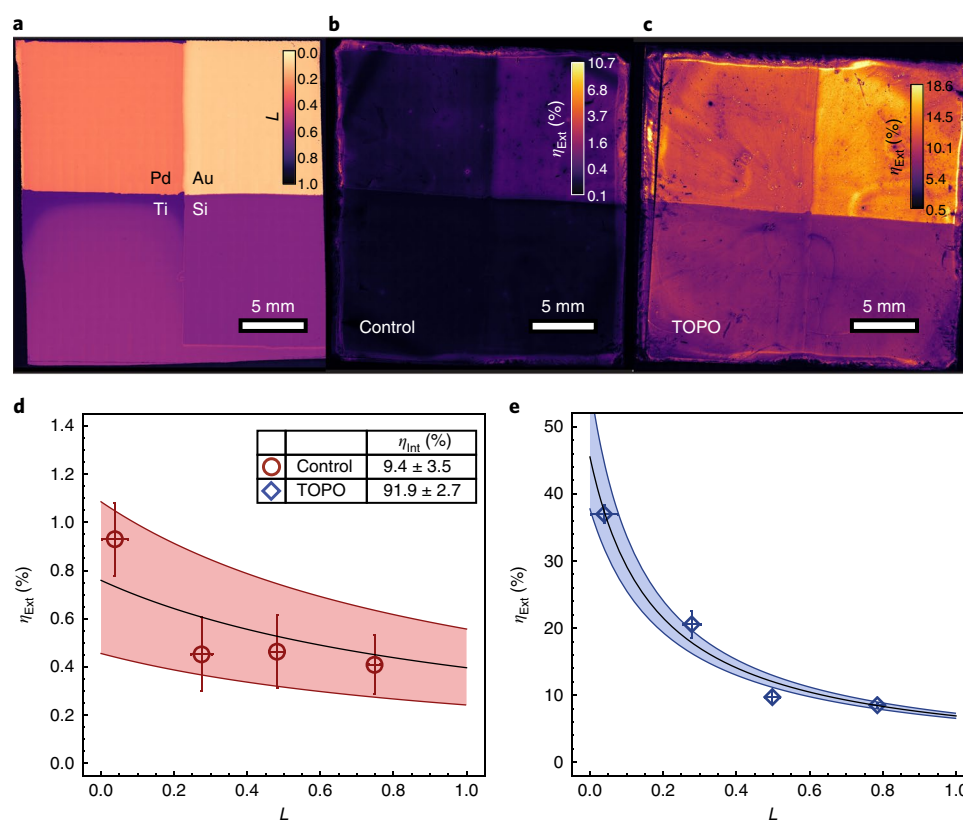


**Fig. 3 | Determination of internal PLQE of surface-passivated perovskite film on a substrate with varying back-surface parasitic absorption.** **a**, Spatial map showing measured optical loss factors,  $L = 1 - \text{Reflectivity} = 1 - R$ , of the Au, Pd, Ti and Si quadrants of the metal back-reflector substrate before perovskite deposition. **b,c**, Spatial map showing  $\eta_{\text{ext}}$  for a typical control (**b**) and TOPO-treated (**c**) film deposited on the multi-metal back-reflector substrate. **d,e**,  $\eta_{\text{ext}}$  data as a function of  $L$  for a control film and champion TOPO-treated film, respectively. Error bars, shaded areas and black lines are 95% confidence intervals over the spatial heterogeneity in the data points, 95% confidence intervals of the nonlinear regression, and nonlinear regression fits, respectively.

(Supplementary Section 8 and Supplementary Fig. 16). Figure 3a presents an image of the loss factors for each metal, where we measure  $L = 0.039 \pm 0.036$  for Au,  $0.278 \pm 0.024$  for Pd,  $0.498 \pm 0.021$  for Ti, and  $0.785 \pm 0.017$  for Si (95% confidence intervals for  $N > 1,000$  within the sample). We also measure  $\eta_{\text{ext}}$  for our samples, independently from the confocal measurements, using an integrating sphere, which we confirmed to be calibrated by measuring a rhodamine 6G standard (Supplementary Fig. 6). For the sample measured in Fig. 1, we independently determined  $\eta_{\text{ext}} = 23.5\%$ , which is within the confidence interval of  $20.3 \pm 5.6\%$  measured using the confocal instrument.

Figure 3b presents a representative  $\eta_{\text{ext}}$  image of a control film subsequently treated with TOPO (Fig. 3c) on a multi-metal back-reflector substrate when measured at 1 Sun equivalent photon flux (532 nm,  $60 \text{ mW cm}^{-2}$ ). As expected, we find that the regions with the smallest parasitic absorption (lowest  $L$ ), exhibit the highest  $\eta_{\text{ext}}$ , and TOPO passivation improves  $\eta_{\text{ext}}$  across the entire substrate (Fig. 3c). Figure 3d,e shows the control and champion TOPO-passivated films on the multi-metal substrates, where the TOPO-passivated film demonstrates a maximum  $\eta_{\text{ext}}$  of  $36.7 \pm 1.4\%$ . We note that, compared to the control sample, the TOPO-passivated sample exhibits a stronger dependence of  $\eta_{\text{ext}}$  on loss factor, which implies that parasitic absorption dominates over non-radiative recombination within the perovskite layer. We used the progression in  $\eta_{\text{ext}}$  values together with equation (2) to extract the  $\eta_{\text{int}}$  values. Surprisingly, we report an order-of-magnitude improvement from  $\eta_{\text{int}} = 9.4 \pm 3.5\%$  for the control sample to  $\eta_{\text{int}} = 91.9 \pm 2.7\%$  for the TOPO-treated film.

The  $\eta_{\text{int}}$  of the control is consistent with other reports for unpassivated perovskite thin films measured at 1 Sun equivalent photon flux<sup>7,22</sup>, whereas the surface-treated film exhibits an internal quantum efficiency only observed in fluorescent molecules containing no dangling bonds<sup>38</sup> as well as just a few semiconducting materials such as GaAs double heterostructures<sup>20</sup>, surface-passivated and core/shell quantum dots, and chemically passivated  $\text{MoS}_2$  (ref. 14).

### Impact of excitation intensity and temperature on PLQE

To confirm that these TOPO-passivated films indeed exhibit  $\eta_{\text{int}}$  values approaching unity, we tested whether non-radiative recombination could be further reduced in these films by performing both excitation- and temperature-dependent measurements. It has previously been shown in perovskite materials that  $\eta_{\text{ext}}$  increases as a function of excitation power due to the increasing fraction of radiative bimolecular recombination over non-radiative, trap-assisted recombination<sup>9,39,40</sup>. In particular, it has been shown that  $\eta_{\text{int}}$  as high as 70% could be achieved at carrier densities of  $\sim 1 \times 10^{17} \text{ cm}^{-3}$  ( $\sim 100$  Suns)<sup>7</sup> and others have shown maximum values in excess of 30%<sup>24,40</sup>. In the ideal material, radiative recombination should no longer be limited by traps, and  $\eta_{\text{int}}$  should be near unity across all carrier densities until non-radiative multi-body effects (that is, Auger recombination) start to dominate at higher carrier concentrations<sup>14</sup>.

In this regard, we tested the excitation-dependent behaviour of TOPO-passivated films. Figure 4a shows the  $\eta_{\text{ext}}$  of a control and TOPO-treated film measured in an integrating sphere as a function of excitation power. For the control film, and consistent with literature



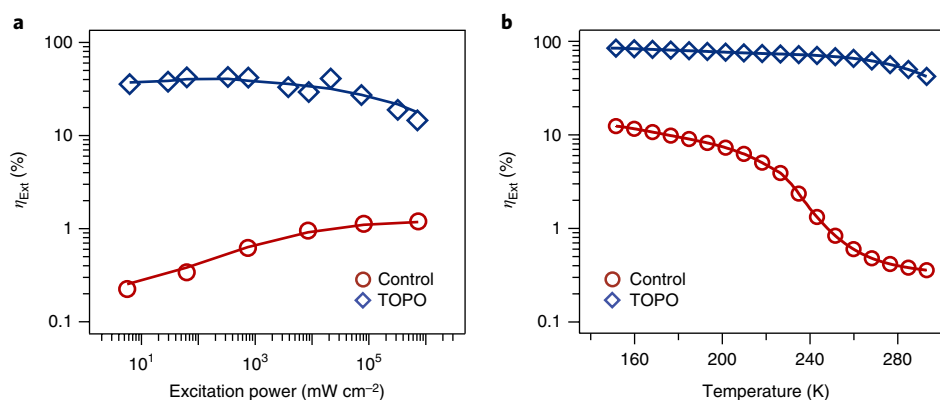


**Fig. 4 | Photoluminescence spectroscopy measurements to determine the maximum achievable quantum efficiency under high excitation powers and low temperatures. a,** Log-log plot of intensity-dependent  $\eta_{\text{ext}}$  for a control and TOPO-treated film at room temperature, showing maximum  $\eta_{\text{ext}}$  values of 1.2% and 43%, respectively. **b,** Semi-log plot of temperature-dependent  $\eta_{\text{ext}}$  for the same control and TOPO-treated films. Linear plots of the data are reported in Supplementary Fig. 18.

reports<sup>7</sup>,  $\eta_{\text{ext}}$  increases steadily as a function of excitation power and reaches a maximum  $\eta_{\text{ext}}$  ( $\eta_{\text{int}}$ ) of 1% (12%) at  $738 \text{ W cm}^{-2}$ , where  $\eta_{\text{int}}$  is predicted using equation (2). On the other hand, the optimized, TOPO-passivated film already demonstrates high  $\eta_{\text{ext}}$  even at very low excitation powers ( $\eta_{\text{ext}} = 36\%$ ,  $6 \text{ mW cm}^{-2}$ ,  $\sim 0.1$  Suns), and only slightly increases from the 1 Sun condition to 43% (94%) at an excitation of  $332 \text{ mW cm}^{-2}$  ( $\sim 5$  Suns), whereupon Auger recombination starts to dominate at subsequent excitation powers (Supplementary Sections 9 and 10 and Supplementary Figs. 17–19). For high-quality perovskite films, the observation that Auger recombination starts to dominate shortly after 1 Sun equivalent photon flux ( $60 \text{ mW cm}^{-2}$ ) is important as it places these films in a favourable regime where the highest radiative efficiencies are achievable under AM1.5 (in contrast to Si)<sup>15</sup>, although we note that this observation may reduce the theoretical performance of the application of perovskites in concentrator photovoltaics (Supplementary Fig. 20)<sup>41</sup>.

Aside from improving  $\eta_{\text{int}}$  by increasing the fraction of radiative recombination by trap-filling at higher excitation powers, other reports have shown that cooling the sample can also achieve a reduction in non-radiative recombination, with maximum  $\eta_{\text{ext}}$  values approaching unity at the lowest temperatures<sup>42</sup>. Figure 4b shows  $\eta_{\text{ext}}$  as a function of temperature of the control and TOPO-passivated films measured at  $60 \text{ mW cm}^{-2}$  and within the tetragonal phase<sup>43</sup>. This control film started at a modest  $\eta_{\text{ext}}$  ( $\eta_{\text{int}}$ ) of 0.3% (4%) at 300 K, which steadily increased to 2% (22%) at 235 K. These improvements correspond to a fivefold enhancement in  $\eta_{\text{ext}}$ , which is consistent with other unpassivated films reported in the literature<sup>40</sup>. The TOPO-treated film, on the other hand, only demonstrated moderate improvements in  $\eta_{\text{ext}}$  ( $\eta_{\text{int}}$ ), ranging from 42% (93%) at 300 K to 70% (99%) at 235 K, an improvement factor below 2 for  $\eta_{\text{ext}}$ , which is consistent with extremely low levels of non-radiative recombination at room temperature under a generation rate comparable to 1 Sun illumination. We note that at temperatures below 235 K, we begin to observe reversible changes in film morphology (Supplementary Section 11 and Supplementary Fig. 21), which suggests that the outcoupling efficiency may be changing and that our calculation of  $\eta_{\text{int}}$  may not be reliable below these temperatures. The comparatively small improvements in the TOPO-treated film as temperature decreases suggests that some thermally activated non-radiative recombination still exists, but whether these recombination centres reside at the surface or are concentrated within the bulk remains an open question.

## Discussion

Considering the history of the development of other successful photovoltaic technologies such as Si and GaAs, surface passivation

appears to be a prerequisite in achieving the highest-quality materials<sup>26,27</sup>. For example, untreated GaAs, Si and CdTe all exhibit high surface recombination velocities due to the presence of dangling bonds and surface oxides, and these surface recombination centres must be passivated to realize high-efficiency devices. Interestingly, initial passivating strategies for GaAs also utilized Lewis bases to significantly reduce the surface recombination velocity<sup>44,45</sup>. Similarly, the passivation of the front and back surfaces of silicon took decades to master<sup>26</sup>, and these foundational studies of tailoring the surface chemistry have allowed silicon to be successful in a wide range of applications. In this study we show, from a purely materials standpoint, that surface-passivated perovskites can achieve  $\Delta\mu$  values approaching the radiative limit, and demonstrate the lowest thermodynamic loss of any perovskite films or devices we are aware of to date. Notably, these values are beginning to approach those of high-quality passivated GaAs. To illustrate this point, we calculated current–voltage curves using the non-radiative monomolecular, radiative bimolecular and Auger trimolecular rate constants<sup>29</sup> calculated for the films we report in the Supplementary Information (Supplementary Section 9 and Supplementary Table 5). The untreated film, assuming a film thickness of 250 nm and ideal contacts, is predicted to enable a power conversion efficiency of 24.3%,  $V_{\text{OC}}$  of 1.18 V, and fill factor of 82.5%, in agreement with both our quasi-Fermi-level splitting results and top-tier devices reported so far. A passivated film such as the one we demonstrate here is predicted to enable significant improvements in power conversion efficiency,  $V_{\text{OC}}$  and fill factor to 27.9%, 1.28 V and 86.9%, respectively (see Supplementary Section 12 and Supplementary Figs. 22 and 23 for JV calculation details and the resulting device figures of merit). As a proof of concept, these results are promising, but we note that achieving these device metrics will probably require careful deposition of a monolayer of non-labile passivating molecules, a detailed understanding of the impact of surface modifiers on band bending and workfunction<sup>46</sup>, and treatments that either maintain or improve conductivity. For example, we have recently shown that while many passivating molecules improve PLQE, some treatment procedures result in the impediment of lateral charge transport<sup>47</sup>. Here, we find that the TOPO surface passivation qualitatively improves the transport length (Supplementary Section 13 and Supplementary Fig. 24), and whether this simply results from longer photocarrier lifetimes, better diffusion across insulating grain boundaries<sup>48</sup>, or more efficient photon recycling will form topics for further study.

In addition to these encouraging results, the  $\Delta\mu$  and  $\eta_{\text{int}}$  observed in this report suggest that the recently proposed direct–indirect nature of the bandgap and observation of band-tail recombination

may not limit the radiative efficiency as previously predicted<sup>49–51</sup>. For example, the indirect nature of the bandgap and Auger recombination in Si limit the internal PLQE to about 20% (ref. 17). This is often attributed to the optical transitions requiring phonons, and thus loss of some energy to lattice vibrations<sup>17</sup>. It has been reported by several groups that photoexcitation in perovskites occurs via a direct transition, and recombination occurs via an indirect transition ~25–75 meV below the direct transition. This band structure has been predicted to reduce the maximum achievable internal PLQE by 50% (ref. 49) and reduce the average bimolecular recombination rate, which reduces  $V_{OC}$  (ref. 50). More recently, it has been proposed that the indirect gap does not significantly contribute to carrier recombination in perovskite films, and instead recombination is dominated by a tail of radiative band states due to disorder<sup>51</sup>. We note that despite the possibility of an indirect transition for recombination in  $\text{CH}_3\text{NH}_3\text{PbI}_3$ , the internal quantum yield approaches unity under 1 Sun conditions, and  $\Delta\mu$  approaches its radiative limit, as predicted by the absorption coefficient (Supplementary Fig. 2). This suggests that with significant reductions in non-radiative recombination, perovskite materials are not limited in reaching the radiative efficiencies of direct-gap semiconductors such as GaAs.

In summary, we provide the first experimental evidence that polycrystalline, solution-processed perovskite ( $\text{CH}_3\text{NH}_3\text{PbI}_3$ ) thin films can achieve internal PLQEs over 90%, and  $\Delta\mu$  as high as  $1.28 \pm 0.01$  eV with careful control of the non-radiative losses that dominate at the surfaces. These values are approaching the theoretical open-circuit voltages predicted by the radiative limit (1.32 V) of a material with a bandgap of 1.60 eV and are highly encouraging, considering that state-of-the-art devices only exhibit  $V_{OC}$  values ~1.15 V. As these high values of  $\Delta\mu$  are only possible with ultra-high external and internal PLQEs, we confirmed our measured values by both directly measuring  $\eta_{ext}$  and implementing a straightforward strategy for determining  $\eta_{int}$ . We believe this method will be highly useful for future studies where only  $\eta_{ext}$  and the loss factors of the substrates will need to be measured. Using this method, we report the highest  $\eta_{int}$  values ( $91.9 \pm 2.7\%$ ) achieved so far in perovskite thin films with 1 Sun equivalent photon flux. This observation places these films among the most emissive semiconducting materials ever fabricated, including GaAs heterostructures and well-passivated quantum dots. Importantly, these findings suggest that there should be no limitations preventing perovskites from approaching the radiative limit under 1 Sun illumination conditions and that these types of surface passivation protocol can be widely implemented in the fabrication of highly efficient light-emitting diodes, low-power optically and electrically driven lasing, and potentially in optical refrigeration applications. By careful control over surface chemistry and the use of charge-selective contacts, it is expected that we will see the desired improvements in the next generation of high-open-circuit-voltage devices with record power conversion efficiencies.

## Methods

Methods, including statements of data availability and any associated accession codes and references, are available at <https://doi.org/10.1038/s41566-018-0154-z>.

Received: 4 September 2017; Accepted: 14 March 2018;  
Published online: 30 April 2018

## References

- Sutherland, B. R. & Sargent, E. H. Perovskite photonic sources. *Nat. Photon.* **10**, 295–302 (2016).
- Zhang, W., Eperon, G. E. & Snaith, H. J. Metal halide perovskites for energy applications. *Nat. Energy* **1**, 16048 (2016).
- De Wolf, S. et al. Organometallic halide perovskites: sharp optical absorption edge and its relation to photovoltaic performance. *J. Phys. Chem. Lett.* **5**, 1035–1039 (2014).
- Stranks, S. D. et al. Electron–hole diffusion lengths exceeding 1 micrometer in an organometal trihalide perovskite absorber. *Science* **342**, 341–344 (2013).
- deQuilettes, D. W. Photoluminescence lifetimes exceeding 8  $\mu\text{s}$  and quantum yields exceeding 30% in hybrid perovskite thin films by ligand passivation. *ACS Energy Lett.* **1**, 438–444 (2016).
- Herz, L. M. Charge-carrier mobilities in metal halide perovskites: fundamental mechanisms and limits. *ACS Energy Lett.* **2**, 1539–1548 (2017).
- Richter, J. M. et al. Enhancing photoluminescence yields in lead halide perovskites by photon recycling and light out-coupling. *Nat. Commun.* **7**, 13941 (2016).
- Tress, W. Perovskite solar cells on the way to their radiative efficiency limit—insights into a success story of high open-circuit voltage and low recombination. *Adv. Energy Mater.* **7**, 1602358 (2017).
- Deschler, F. et al. High photoluminescence efficiency and optically pumped lasing in solution-processed mixed halide perovskite semiconductors. *J. Phys. Chem. Lett.* **5**, 1421–1426 (2014).
- Tvingstedt, K. et al. Radiative efficiency of lead iodide based perovskite solar cells. *Sci. Rep.* **4**, 6071 (2014).
- Shockley, W. & Queisser, H. J. Detailed balance limit of efficiency of p–n junction solar cells. *J. Appl. Phys.* **32**, 510–519 (1961).
- Rau, U. Reciprocity relation between photovoltaic quantum efficiency and electroluminescent emission of solar cells. *Phys. Rev. B* **76**, 085303 (2007).
- Katahara, J. K. & Hillhouse, H. W. Quasi-Fermi level splitting and sub-bandgap absorptivity from semiconductor photoluminescence. *J. Appl. Phys.* **116**, 173504 (2014).
- Amani, M. et al. Near-unity photoluminescence quantum yield in  $\text{MoS}_2$ . *Science* **350**, 1065–1068 (2015).
- Tiedje, T., Yablonovitch, E., Cody, G. D. & Brooks, B. G. Limiting efficiency of silicon solar cells. *IEEE Trans. Electron. Devices* **31**, 711–716 (1984).
- Green, M. A. et al. Solar cell efficiency tables (version 49). *Prog. Photovolt. Res. Appl.* **25**, 3–13 (2017).
- Trupke, T. et al. Very efficient light emission from bulk crystalline silicon. *Appl. Phys. Lett.* **82**, 2996–2998 (2003).
- Yao, J. et al. Quantifying losses in open-circuit voltage in solution-processable solar cells. *Phys. Rev. Appl.* **4**, 014020 (2015).
- Miller, O. D., Yablonovitch, E. & Kurtz, S. R. Strong internal and external luminescence as solar cells approach the Shockley–Queisser limit. *IEEE J. Photovolt.* **2**, 303–311 (2012).
- Schnitzer, I., Yablonovitch, E., Caneau, C. & Gmitter, T. J. Ultra-high spontaneous emission quantum efficiency, 99.7% internally and 72% externally, from  $\text{AlGaAs/GaAs/AlGaAs}$  double heterostructures. *Appl. Phys. Lett.* **62**, 131–133 (1993).
- Correa-Baena, J. P. et al. Promises and challenges of perovskite solar cells. *Science* **358**, 739–744 (2017).
- Pazos-Outon, L. M. et al. Photon recycling in lead iodide perovskite solar cells. *Science* **351**, 1430–1433 (2016).
- Yang, Y. et al. Top and bottom surfaces limit carrier lifetime in lead iodide perovskite films. *Nat. Energy* **2**, 16207 (2017).
- Noel, N. K. et al. Enhanced photoluminescence and solar cell performance via Lewis base passivation of organic–inorganic lead halide perovskites. *ACS Nano* **8**, 9815–9821 (2014).
- Stewart, R. J. et al. Approaching bulk carrier dynamics in organo-halide perovskite nanocrystalline films by surface passivation. *J. Phys. Chem. Lett.* **7**, 1148–1153 (2016).
- Aberle, A. G. Surface passivation of crystalline silicon solar cells: a review. *Prog. Photovolt. Res. Appl.* **8**, 473–487 (2000).
- Bertness, K. A. et al. 29.5%-efficient  $\text{GaInP/GaAs}$  tandem solar cells. *Appl. Phys. Lett.* **65**, 989–991 (1994).
- Zheng, X. et al. Defect passivation in hybrid perovskite solar cells using quaternary ammonium halide anions and cations. *Nat. Energy* **2**, 17102 (2017).
- Pazos-Outon, L. M., Xiao, T. P. & Yablonovitch, E. Fundamental efficiency limit of lead iodide perovskite solar cells. *J. Phys. Chem. Lett.* **9**, 1703–1711 (2018).
- Kirchartz, T., Staub, F. & Rau, U. Impact of photon recycling on the open-circuit voltage of metal halide perovskite solar cells. *ACS Energy Lett.* **1**, 731–739 (2016).
- Yablonovitch, E., Miller, O. D. & Kurtz, S. R. The opto-electronic physics that broke the efficiency limit in solar cells. *38th IEEE Photovoltaic Specialists Conference* 001556–001559 (IEEE, 2012).
- Zhang, W. et al. Ultrasoft organic–inorganic perovskite thin-film formation and crystallization for efficient planar heterojunction solar cells. *Nat. Commun.* **6**, 6142 (2015).
- Saliba, M. et al. Incorporation of rubidium cations into perovskite solar cells improves photovoltaic performance. *Science* **354**, 206–209 (2016).
- Bauer, G. H., Brüggemann, R., Tardon, S., Vignoli, S. & Kniese, R. Quasi-Fermi level splitting and identification of recombination losses from room temperature luminescence in  $\text{Cu}(\text{In}_{1-x}\text{Ga}_x)\text{Se}_2$  thin films versus optical band gap. *Thin Solid Films* **480**, 410–414 (2005).

35. Ross, R. T. Some thermodynamics of photochemical systems. *J. Chem. Phys.* **46**, 4590–4593 (1967).
36. deQuilettes, D. W. et al. Impact of microstructure on local carrier lifetime in perovskite solar cells. *Science* **348**, 683–686 (2015).
37. Kayes, B. M. et al. 27.6% conversion efficiency, a new record for single-junction solar cells under 1 sun illumination. *37th IEEE Photovoltaic Specialists Conference* 000004–000008 (IEEE, 2011).
38. Drexhage, K. H. Fluorescence efficiency of laser dyes. *J. Res. Natl Bur. Stand. A* **80A**, 421 (1976).
39. Johnston, M. B. & Herz, L. M. Hybrid perovskites for photovoltaics: charge-carrier recombination, diffusion, and radiative efficiencies. *Acc. Chem. Res.* **49**, 146–154 (2016).
40. Stranks, S. D. et al. Recombination kinetics in organic-inorganic perovskites: excitons, free charge, and subgap states. *Phys. Rev. Appl.* **2**, 034007 (2014).
41. Lin, Q. et al. Hybrid perovskites: prospects for concentrator solar cells. *Adv. Sci.* **2018**, 1700792 (2018).
42. Stranks, S. D. Nonradiative losses in metal halide perovskites. *ACS Energy Lett.* **2**, 1515–1525 (2017).
43. Stoumpos, C. C., Malliakas, C. D. & Kanatzidis, M. G. Semiconducting tin and lead iodide perovskites with organic cations: phase transitions, high mobilities, and near-infrared photoluminescent properties. *Inorg. Chem.* **52**, 9019–9038 (2013).
44. Sandroff, C. J., Nottenburg, R. N., Bischoff, J. C. & Bhat, R. Dramatic enhancement in the gain of a GaAs/AlGaAs heterostructure bipolar transistor by surface chemical passivation. *Appl. Phys. Lett.* **51**, 33–35 (1987).
45. Yablonovitch, E., Sandroff, C. J., Bhat, R. & Gmitter, T. Nearly ideal electronic properties of sulfide coated GaAs surfaces. *Appl. Phys. Lett.* **51**, 439–441 (1987).
46. Kesting, K. M. et al. ITO interface modifiers can improve  $V_{oc}$  in polymer solar cells and suppress surface recombination. *J. Phys. Chem. Lett.* **4**, 4038–4044 (2013).
47. Stoddard, R. J., Eickemeyer, F. T., Katahara, J. K. & Hillhouse, H. W. Correlation between photoluminescence and carrier transport and a simple in-situ passivation method for high-bandgap hybrid perovskites. *J. Phys. Chem. Lett.* **8**, 3289–3298 (2017).
48. deQuilettes, D. W. et al. Tracking photoexcited carriers in hybrid perovskite semiconductors: trap-dominated spatial heterogeneity and diffusion. *ACS Nano* **11**, 11488–11496 (2017).
49. Wang, T. et al. Indirect to direct bandgap transition in methylammonium lead halide perovskite. *Energy Environ. Sci.* **10**, 509–515 (2017).
50. Kirchartz, T. & Rau, U. Decreasing radiative recombination coefficients via an indirect band gap in lead halide perovskites. *J. Phys. Chem. Lett.* **8**, 1265–1271 (2017).
51. Wright, A. D. et al. Band-tail recombination in hybrid lead iodide perovskite. *Adv. Funct. Mater.* **27**, 1700860 (2017).

## Acknowledgements

D.W.D. and D.S.G. acknowledge the US Department of Energy (DOE) (DE-SC0013957) for supporting the microscopy work. D.W.D. acknowledges support from an NSF Graduate Research Fellowship (DGE-1256082) and thanks L. Flagg for experimental help. I.L.B. and H.W.H. acknowledge financial support from the US DOE SunShot Initiative, Next Generation Photovoltaics 3 program, Award DE-EE0006710. Part of this work was conducted at the Molecular Analysis Facility and at the Washington Nanofabrication Facility, two National Nanotechnology Coordinated Infrastructure sites at the University of Washington, which are supported in part by the NSF (grant no. ECC-1542101), the University of Washington, the Molecular Engineering and Sciences Institute, the Clean Energy Institute and the National Institutes of Health. L.M.P.-O was supported by the Kavli Energy NanoScience Institute Heising-Simons Junior Fellowship of the University of California, Berkeley. The authors acknowledge F. Deschler for his helpful discussions.

## Author contributions

The project was conceived, planned and coordinated by D.W.D., I.L.B., H.W.H. and D.S.G. Samples were prepared by I.L.B., D.W.D. and S.B. Absolute-intensity photoluminescence spectra and fits were completed by I.L.B. Integrating sphere measurements were conducted by D.W.D. Intensity and temperature-dependent measurements were collected by I.L.B. and D.W.D. L.M.P.-O assisted in extracting the internal PLQE and calculating photovoltaic device metrics. M.E.Z. performed ellipsometry measurements and analysis. All authors assisted in the interpretation of results. D.W.D. and I.L.B. wrote the manuscript, and all authors helped with editing.

## Competing interests

The authors declare no competing interests.

## Additional information

**Supplementary information** is available for this paper at <https://doi.org/10.1038/s41566-018-0154-z>.

**Reprints and permissions information** is available at [www.nature.com/reprints](http://www.nature.com/reprints).

**Correspondence and requests for materials** should be addressed to D.S.G. or H.W.H.

**Publisher's note:** Springer Nature remains neutral with regard to jurisdictional claims in published maps and institutional affiliations.

## Methods

**Perovskite precursor preparation.** A methylammonium iodide (MAI) stock solution was made by dissolving MAI (Dyesol, CAS:14965-49-2) in anhydrous *N,N*-dimethylformamide (DMF) at a concentration of 1.78 M. Lead acetate trihydrate (99.999%, Sigma-Aldrich, CAS:6080-56-4) was then added at a 3:1 molar ratio of MAI to  $\text{PbOAc}_2 \cdot 3\text{H}_2\text{O}$  (0.59 M)<sup>32</sup>. All solutions were made in a nitrogen-filled glovebox.

**Perovskite deposition.** Patterned back-reflector substrates were prepared by electron-beam evaporation on polished silicon wafers using laser-cut polyethylene terephthalate (PET) masks. An adhesion layer of titanium was deposited (10 nm) before depositing 100 nm of gold. All other metals were deposited directly on the silicon native oxide layer at a thickness of 100 nm. A 230 nm film of  $\text{SiO}_2$  was electron-beam-evaporated on the entire patterned wafer as an insulating layer.

To form the perovskite layer for spectroscopy measurements, the precursor solutions were spin-coated on plasma-cleaned substrates at 2,000 r.p.m. for 60 s. Films were left to dry at room temperature for 10 min and then annealed on a hotplate at 100 °C for 5 min. The spin-coating, room-temperature drying and hotplate anneal were all carried out in a nitrogen-filled glovebox.

**Surface treatment deposition.** TOPO (Sigma, CAS: 78-50-2) treatment solutions were prepared in anhydrous chlorobenzene (Sigma-Aldrich, CAS: 108-90-7) with a concentration of 0.025 M. Treatments were carried out by depositing ~200  $\mu\text{l}$  of the treatment solution on the film, then immediately spin-coating at 2,000 r.p.m. for 60 s. Multiple treatments (~3) were often performed without a washing step to achieve the largest enhancements (Supplementary Fig. 14).

**Absolute intensity photoluminescence measurement.** Bulk photoluminescence measurements were collected using a modified Horiba LabRAM HR-800 and an upright microscope fitted with a 10 $\times$  objective (Olympus M Plan achromat, NA 0.25). The adjustable confocal hole before the monochromator was set at 800  $\mu\text{m}$ . A 150 gr/mm Czerny–Turner monochromator blazed at 1,200 nm was used, and the emitted light was collected with a silicon charge-coupled device array detector. The photoluminescence signal was calibrated using a black-body source (IR-301, Infrared Systems Development Corporation) at a temperature of 1,323.15 K. A 100- $\mu\text{m}$ -diameter pinhole was used to fix the spectral photon black-body flux to the detector and allow an absolute-photons-per-count calibration factor to be measured (Supplementary Section 5). A 532 nm continuous-wave (c.w.) laser was used for excitation. An Oriel optical power meter was used to measure the illumination intensity and excitation diameter. An excitation power of 60 mW  $\text{cm}^{-2}$  was used, equivalent to the photon flux absorbed at 1 Sun illumination for a 1.6 eV bandgap material<sup>32</sup>.

**External PLQE measurement.** External PLQE measurements were acquired using an integrating sphere set-up (Hamamatsu C9920-02, A10094). A 532 nm c.w. laser (CrystaLaser, GCL532-005-L) was used to excite the sample, and neutral density filters were used to attenuate the laser for intensity-dependent measurements. Data acquisition followed the protocol described in ref.<sup>53</sup>.

**Wide-field, bright-field and photoluminescence imaging.** Reflectivity and external PLQE images were collected with an Olympus BX53M microscope equipped with a motorized *XY* translation stage, motorized *z*-axis controller, 10 $\times$  objective lens (Olympus MPlanFL N) and a CMOS camera (Hamamatsu C11440 Orca Flash 4.0). A 790 nm LED (Lumencor SpectraX-LCR-6N-B1) was used for reflectivity (for spectrum see Supplementary Fig. 16), and the pixel values were calibrated using a gold mirror. A 545 nm LED (Lumencor), 665 nm dichroic beamsplitter and a 664 nm long-pass filter were used for fluorescence images. The pixel value of each sample was calibrated by measuring the external PLQE of each region of different back-surface reflectivity in an integrating sphere directly after imaging. The total illumination intensity and distribution of the incident light were measured using a beam profiler (Thorlabs BP209-VIS) and an optical power meter (Oriel), respectively. Images were flattened using an average dark image and a mean image of several rhodamine 6G in ethanol fluorescence images ( $N=100$ ) utilizing the Micromanager On-the-fly image flattening plugin on ImageJ<sup>54</sup>. Images were stitched together using the overlap averaging method in the MIST<sup>55</sup> ImageJ<sup>56</sup> plugin.

**Data availability.** The data that support the plots within this paper and other findings of this study are available from the corresponding author upon reasonable request.

## References

52. Ziffer, M. E., Mohammed, J. C. & Ginger, D. S. Electroabsorption spectroscopy measurements of the exciton binding energy, electron–hole reduced effective mass, and band gap in the perovskite  $\text{CH}_3\text{NH}_3\text{PbI}_3$ . *ACS Photon.* **3**, 1060–1068 (2016).
53. de Mello, J. C., Wittmann, H. F. & Friend, R. H. An improved experimental determination of external photoluminescence quantum efficiency. *Adv. Mater.* **9**, 230–232 (1997).
54. Edelstein, A. D. et al. Advanced methods of microscope control using  $\mu$  Manager software. *J. Biol. Methods* **1**, e10 (2014).
55. Blattner, T. et al. A hybrid CPU–GPU system for stitching large scale optical microscopy images. *43rd International Conference on Parallel Processing* (IEEE, 2014).
56. Schindelin, J. et al. Fiji: an open-source platform for biological-image analysis. *Nat. Methods* **9**, 676–682 (2012).